

---

## Hidefumi Wakamatsu

Department of Manufacturing Science  
Graduate School of Engineering  
Osaka University  
Suita, Osaka 565-0871, Japan

## Shinichi Hirai

Department of Robotics  
Ritsumeikan University  
Kusatsu, Shiga 525-8577, Japan

# Static Modeling of Linear Object Deformation Based on Differential Geometry

## Abstract

*We describe the modeling of linear object deformation based on differential geometry and its applications to manipulative operations. A particle-based approach, the finite element method, and the Cosserat theory have been applied to the modeling of linear object deformation. In this paper, we establish an alternative modeling approach based on an extension of differential geometry. First, we extend differential geometry to describe linear object deformation including flexure, torsion, and extension. Secondly, we show computational results to demonstrate the feasibility of the proposed modeling technique, and we compare computational and experimental results to demonstrate the accuracy of the model. Next, we apply the proposed approach to the grasping of a deformable linear object. We propose a disturbance force margin to indicate the stability of the grasping and we describe the computation of the margin using the proposed approach. Finally, we apply the proposed approach to the deformation path planning of a linear object. We formulate the minimization of potential energy during a deformation path. We compute the optimal deformation path and a feasible deformation path, which are compared with an experimental result.*

**KEY WORDS**—deformation, modeling, linear objects, statics, differential geometry

## 1. Introduction

Many manipulative operations deal with deformable linear objects such as wires, cords, and threads with flexural, torsional, and extensional deformations in three-dimensional (3D) space. For example, electrical and optical cables are manipulated in the building and maintenance of communication systems, wires and cables are manipulated in the manufac-

turing of electrical apparatuses and automobiles, and medical threads are used in surgery. Linear objects are defined as objects that are much larger along one of the orthogonal directions than along the other two. Modeling of linear object deformation is required for many purposes, including planning of manipulative operations and design of products.

In this paper, we describe the modeling of linear object deformation based on differential geometry and its applications to manipulative operations. Much research has been done on the modeling of linear object deformation; a particle-based approach, the finite element method (FEM), and the Cosserat theory have been applied to the modeling. We establish an alternative modeling approach based on an extension of differential geometry. First, we extend differential geometry to describe linear object deformation including flexure, torsion, and extension. This follows on from a method that we previously proposed for describing linear object deformation intuitively (Wakamatsu, Hirai, and Iwata 1995; Hirai 2000). Here, we will focus on a mathematical description based on differential geometry. Secondly, we show computational results to demonstrate the feasibility of the proposed modeling method. Since planning of manipulative operations and design of products require that the model be accurate, we compare computational and experimental results to demonstrate the accuracy. Next, we apply the proposed approach to manipulative operations of deformable linear objects, i.e., grasping and deformation path planning. We propose a disturbance force margin to indicate the stability of the grasping and describe the computation of the margin using the proposed approach. In deformation path planning, we compute the optimal deformation path and a feasible deformation path using the proposed approach.

### 1.2. Related Work

Solid mechanics has been studied for a long time to formulate the deformation of solid bodies (Fung 1965). Solid

mechanics basically focuses on the local deformation of solid bodies rather than the global deformation of objects. Modeling of global object deformation has been extensively studied in computer graphics and virtual reality. Elasticity theory has been applied to physically based modeling of deformable objects (Terzopoulos et al. 1987; Terzopoulos and Witkin 1988). The introduction of the FEM has extended these studies. Geometrically-nonlinear FEM has been applied to the modeling of global deformation with real-time haptic rendering (Zhuang and Canny 2000). Rotation-invariant nonlinear FEM has been applied to the modeling of anisotropic soft tissues for real-time simulation (Picinbono, Delingette, and Ayache 2001). Space and time adaptive sampling of multi-resolution hierarchy of tetrahedral meshes with large Green strain formulation has allowed real-time simulation of global object deformation (DeBunne et al. 2001). The boundary element method (BEM) has been introduced to the modeling of deformable objects (James and Pai 1999, 2002). The BEM approach is applicable to only uniform objects, but can reduce the computation time, resulting in real-time simulation of global object deformation. In the particle-based approach, a deformable object is represented by a set of particles connected by mechanical elements (Witkin and Welch 1990), and the penalty method has been proposed to describe the collision among objects (Joukhaider, Deguet, and Laugie 1998).

The high aspect ratio of thin objects, such as paper and cloth, and linear objects, such as wire and thread, often causes instability in the computation of deformed shapes. Thus, various modeling techniques have been adapted for thin or linear objects. For example, the deformed shape of a thread suspended by two points has been analyzed using calculus of variations and it has been found that the shape can be described by a catenary (Irvine 1981). The deformation of clothes has been described using catenaries (Weil 1986). In these approaches, the material properties are not considered; only the mass is considered. Nonlinear shell theory has been applied to the modeling of fabric deformation (Eischen, Deng, and Clapp 1996). A particle-based model of cloth has been proposed for drape simulation (Eberhardt, Weber, and Strasswer 1996). Implicit numerical integration has been introduced to the particle-based cloth model to reduce computation time (Baraff and Witkin 1998). Knot tying of a thread has been simulated using a particle-based model of the thread (Phillips, Ladd, and Kavradi 2002). The deformed shape of threads in a fabric has been described geometrically (Leaf 1960). In computer graphics, the particle-based approach has been applied to simulate the motion of hairs. Flexure and extension of hairs have been described in Rosenblum, Carlson, and Tripp (1991), while flexure and torsion of hairs have been described in Daldegan et al. (1993), implying that flexure, torsion, and extension of a linear object can be described using a particle-based approach. Deformation of a linear object can be modeled using beam elements in the FEM. Spline-based modeling has been applied to the real-time simulation of soft tissues as

well as sutures in surgery (Kühnapfel, Çakmak, and Maass 2000). Linear objects have been approximated using beams in the engineering community; models exist to describe small deflection of beams (Timoshenko 1955), and also large deformation using nonlinear beam finite elements (Belytschko, Liu, and Moran 2000). Recently, fast algorithms have been introduced to describe linear object deformation using the Cosserat formulation (Pai 2002). Cosserat elements possess six degrees of freedom: three for translational displacement and three for rotational displacement. Flexure, torsion, and extension of a linear object can be described by use of Cosserat elements.

Mathematical descriptions of linear objects have been studied in knot theory and differential geometry. Knot theory provides a topological classification and description of knots of a thread (Adams 1994). Language has been designed to describe the transitions among knot topologies during the manipulation of a thread (Hopcroft, Kearney, and Krafft 1991). In differential geometry, curved lines in two-dimensional (2D) or 3D space have been studied to describe their shapes mathematically (Gray 1993). Differential geometry can describe flexure of a linear object, but not extension along or torsion around the object.

Manipulation of deformable objects has been studied in robotics (Taylor 1990; Henrich and Wörn 2000). Insertion of a wire into a hole has been analyzed using a beam model of the wire to derive a strategy to perform the insertion successfully (Zheng, Pei, and Chen 1991; Nakagaki et al. 1997). Vibration-free handling of a beam has been investigated using a beam dynamic model (Chen and Zheng 1995). Sensor-based dynamic insertion of a wire has been investigated (Yue and Henrich 2002). A distributed compliance model has been proposed to describe the assembly of deformable parts (Villarreal and Asada 1991). A particle-based model of fabric has been applied to control the fabric positioning operation (Hirai and Wada 2000). Inverse problems in the manipulation of a linear object have been solved using an object model computed in parallel on a cluster system (Remde and Henrich 2000).

Much research has focused on the modeling of linear object deformation. The particle-based approach, the FEM, and the Cosserat theory have been employed. In this paper, we establish an alternative modeling based on an extension of differential geometry. Mathematical description of a curved line in 3D space has been studied in differential geometry. It is well known that, in differential geometry, any curved line can be specified uniquely by two functions, which implies that flexure of a linear object can be expressed by these two functions. However, extension along and torsion around the curved line cannot be described in differential geometry since these deformations cannot be determined uniquely for any one curved line. Two additional functions need to be introduced to express the extension and torsion of a linear object. Thus, at least four functions are required to describe linear object deformation, i.e., flexure, torsion, and extension. The proposed method describes linear object deformation by four functions.

We often have to manipulate cables or wires composed of several materials. Our model is applicable to the modeling of these objects since flexure, torsion, and extension of the linear object are formulated independently. Thus, we can identify deformation parameters independently and can construct the object model easily. The particle-based approach is also applicable but it requires many more parameters to describe the deformation. Our model is continuous so that deformation can be described by relatively few parameters. These properties are conducive to the planning of manipulative operations of deformable linear objects. Thus, we apply the proposed approach.

## 2. Description of Linear Object Deformation Based on Differential Geometry

### 2.1. Differential Geometry Coordinates

In this section, we formulate the deformation of a linear object in 3D space. As described by Frenet–Serret formulae in differential geometry, any curve in 3D space can be specified by the Frenet frame field (Gray 1993). However, extension along a linear object and torsion around its central axis cannot be described in the Frenet frame field. Instead, we specify the relationship between two frame fields defined in natural and deformed states of a linear object. Let  $L$  be the length of the object and let  $s$  be the distance from one end point of the object along its central axis. Let  $P(s)$  be the point on the object at distance  $s$ . In order to describe the deformation of a linear object, the global space coordinate system and the local object coordinate systems at individual points on the object are introduced as shown in Figure 1. Let  $O - xyz$  be the coordinate system fixed in space and  $P - \xi\eta\zeta$  be the coordinate system fixed at an arbitrary point  $P(s)$  on the object. Assume that the object is straight along the  $z$ -axis in its natural state whereby the object has no deformation. Select the direction of coordinates so that the  $\xi$ -,  $\eta$ -, and  $\zeta$ -axes are parallel to the  $x$ -,  $y$ -, and  $z$ -axes, respectively, in the natural state. Deformation of the object is then represented by the relationship between the local coordinate system  $P - \xi\eta\zeta$  at each point on the object and the global coordinate system  $O - xyz$ . This is referred to as differential geometry coordinate representation.

Let us describe the orientation of the local coordinate system with respect to the space coordinate system by use of Eulerian angles,  $\phi(s)$ ,  $\theta(s)$ , and  $\psi(s)$ . The rotational transformation from the coordinate system  $P - \xi\eta\zeta$  to the coordinate system  $O - xyz$  will be expressed by the following rotation matrix:

$$A(\phi, \theta, \psi) = \begin{bmatrix} \cos \phi & -\sin \phi & 0 \\ \sin \phi & \cos \phi & 0 \\ 0 & 0 & 1 \end{bmatrix}$$

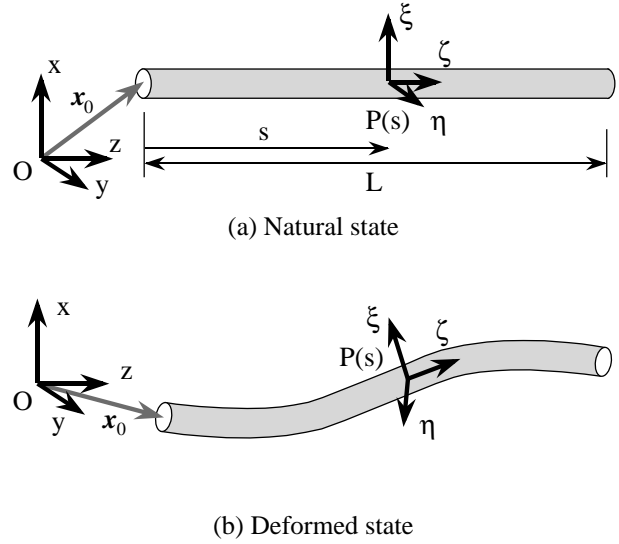


Fig. 1. Coordinate systems describing object deformation.

$$\begin{bmatrix} \cos \theta & 0 & \sin \theta \\ 0 & 1 & 0 \\ -\sin \theta & 0 & \cos \theta \end{bmatrix} \begin{bmatrix} \cos \psi & -\sin \psi & 0 \\ \sin \psi & \cos \psi & 0 \\ 0 & 0 & 1 \end{bmatrix} \\ = \begin{bmatrix} \cos \theta \cos \phi \cos \psi - \sin \phi \sin \psi \\ \cos \theta \sin \phi \cos \psi + \cos \phi \sin \psi \\ -\sin \theta \cos \psi \\ -\cos \theta \cos \phi \sin \psi - \sin \phi \cos \psi \\ -\cos \theta \sin \phi \sin \psi + \cos \phi \cos \psi \\ \sin \theta \sin \psi \end{bmatrix} \begin{bmatrix} \sin \theta \cos \phi \\ \sin \theta \sin \phi \\ \cos \theta \end{bmatrix}. \quad (1)$$

Note that the Eulerian angles depend on distance  $s$ . Let  $\xi$ ,  $\eta$ , and  $\zeta$  be unit vectors along the  $\xi$ -,  $\eta$ -, and  $\zeta$ -axes, respectively, at point  $P(s)$ . These unit vectors are given by the first, second, and third columns of the rotation matrix, respectively. Namely,

$$A(\phi, \theta, \psi) = [ \xi \mid \eta \mid \zeta ].$$

### 2.2. Flexure, Torsion, and Extension of Linear Object

Let us describe the curvature of a deformable linear object and its torsional angle in order to express flexural and torsional deformations of the object. Let  $\omega_\xi$ ,  $\omega_\eta$ , and  $\omega_\zeta$  be infinitesimal ratios of rotation angles around the  $\xi$ -,  $\eta$ -, and  $\zeta$ -axes, respectively, at point  $P(s)$  to distance  $s$ . Since  $\xi$ ,  $\eta$ , and  $\zeta$  are orthonormal vectors, the ratios satisfy the following equation:

$$\begin{bmatrix} \frac{d\xi}{ds} & \frac{d\eta}{ds} & \frac{d\zeta}{ds} \end{bmatrix} = [ \xi \mid \eta \mid \zeta ] \\ \begin{bmatrix} 0 & -\omega_\zeta & \omega_\eta \\ \omega_\zeta & 0 & -\omega_\xi \\ -\omega_\eta & \omega_\xi & 0 \end{bmatrix}.$$

From this equation, we have

$$\begin{bmatrix} 0 & -\omega_\zeta & \omega_\eta \\ \omega_\zeta & 0 & -\omega_\xi \\ -\omega_\eta & \omega_\xi & 0 \end{bmatrix} = A^T \frac{dA}{ds}. \quad (2)$$

Note that the above equation is similar to the relationship between the angular velocity vector and rotation matrix in rigid-body motion. By substituting eq. (1) into the above equation, the infinitesimal angle ratios can be described as follows:

$$\begin{bmatrix} \omega_\xi \\ \omega_\eta \\ \omega_\zeta \end{bmatrix} = \begin{bmatrix} -\sin \theta \cos \psi \\ \sin \theta \sin \psi \\ \cos \theta \end{bmatrix} \frac{d\phi}{ds} + \begin{bmatrix} \sin \psi \\ \cos \psi \\ 0 \end{bmatrix} \frac{d\theta}{ds} + \begin{bmatrix} 0 \\ 0 \\ 1 \end{bmatrix} \frac{d\psi}{ds}.$$

Let  $\kappa$  and  $\omega$  be the curvature and the torsional angle at point  $P(s)$ , respectively. The curvature and torsional angle can then be described using infinitesimal angle ratios as follows:

$$\kappa^2 = \omega_\xi^2 + \omega_\eta^2 = \left(\frac{d\theta}{ds}\right)^2 + \left(\frac{d\phi}{ds}\right)^2 \sin^2 \theta, \quad (3)$$

$$\omega^2 = \omega_\zeta^2 = \left(\frac{d\phi}{ds} \cos \theta + \frac{d\psi}{ds}\right)^2. \quad (4)$$

Note that the curvature  $\kappa$  and the torsional angle  $\omega$  both depend on distance  $s$ . It should be emphasized that, using eq. (2), we can compute infinitesimal ratios  $\omega_\xi$ ,  $\omega_\eta$ , and  $\omega_\zeta$  for any expression of rotation matrix  $A$ . This implies that the above derivation is general and that we can derive the curvature  $\kappa$  and the torsional angle  $\omega$  for any expression of the rotation matrix.

In order to express the extensional deformation of a linear object, a strain at each point  $P(s)$  will be introduced. Let  $\varepsilon$  be extensional strain at point  $P(s)$  on a linear object along its central axis. It turns out that the unit vector along the  $\zeta$ -axis at the natural state can be transformed into the following vector due to the object deformation:

$$(1 + \varepsilon) \boldsymbol{\zeta}(s) = (1 + \varepsilon) \begin{bmatrix} \sin \theta \cos \phi \\ \sin \theta \sin \phi \\ \cos \theta \end{bmatrix}. \quad (5)$$

Let  $\mathbf{x}(s) = [x(s), y(s), z(s)]^T$  be the position vector of point  $P(s)$ . The position vector can be computed by integrating vector  $(1 + \varepsilon) \boldsymbol{\zeta}(s)$ . Namely,

$$\mathbf{x}(s) = \mathbf{x}_0 + \int_0^s (1 + \varepsilon) \boldsymbol{\zeta}(s) ds, \quad (6)$$

where  $\mathbf{x}_0 = [x_0, y_0, z_0]^T$  is the position vector at the end point  $P(0)$ .

From the above discussion, it is found that the geometrical shape of a deformed linear object can be represented by four functions, namely, Eulerian angles  $\phi$ ,  $\theta$ , and  $\psi$ , and extensional strain  $\varepsilon$ . Note that each function depends upon parameter  $s$ .

### 3. Static Modeling of Linear Object Deformation

In this paper, the variational principle in statics are applied to the modeling of linear object deformation. According to this principle, under the imposed constraints, the internal energy of a linear object attains its minimum value in its stable deformed state. Dynamical effects during operations are assumed to be negligible.

#### 3.1. Internal Energy of Linear Object

Let us formulate the potential energy of a deformed linear object and the work done by external forces to express the internal energy of the object. First, the potential energy of a linear object will be formulated. Assume that the thickness and the width of the object are negligible. Applying the assumption of Bernoulli and Navier, it turns out that the potential energy  $U$  can be described as follows

$$U = U_{flex} + U_{tor} + U_{ext} + U_{grav} \quad (7)$$

where  $U_{flex}$ ,  $U_{tor}$ , and  $U_{ext}$  represent the flexural, torsional, and extensional energy of the object, respectively, and  $U_{grav}$  denotes its gravitational energy.

The object's total flexural energy  $U_{flex}$  and total torsional energy  $U_{tor}$  can be computed by integrating, respectively, flexural energy and torsional energy at point  $P(s)$  over the object. Assuming that the flexural energy and the torsional energy are proportional to the bending moment and twisting moment at each point  $P(s)$ , respectively, the energies can be described as follows

$$U_{flex} = \frac{1}{2} \int_0^L R_f \kappa^2 ds, \quad (8)$$

$$U_{tor} = \frac{1}{2} \int_0^L R_t \omega^2 ds \quad (9)$$

where  $R_f$  and  $R_t$  represent the flexural and torsional rigidity at point  $P(s)$ , respectively. Note that  $R_f$  and  $R_t$  may vary with respect to distance  $s$ . Assuming that the extensional energy is proportional to the extensional strain at each point  $P(s)$ , extensional energy  $U_{ext}$  is given by

$$U_{ext} = \frac{1}{2} \int_0^L R_e \varepsilon^2 ds \quad (10)$$

where  $R_c$  denotes the extensional rigidity of the object, which may depend on distance  $s$ . Assuming that gravity forces act along the  $x$ -axis, the gravitational energy is given by

$$U_{grav} = \int_0^L D x \, ds \quad (11)$$

where  $D$  represents weight per unit length of the object. The quantity  $D$  may also vary with distance  $s$ .

Let  $\mathbf{p}_i$  be an external force applied to a linear object at point  $P(s_i)$  and let  $\delta \mathbf{q}_i$  be the resultant displacement of that point. Then, work  $W_i$  done by the external force  $\mathbf{p}_i$  can be described as follows:

$$W_i = \mathbf{p}_i \cdot \delta \mathbf{q}_i. \quad (12)$$

Note that displacement  $\delta \mathbf{q}_i$  can be represented by four variables:  $\phi(s)$ ,  $\theta(s)$ ,  $\psi(s)$ , and  $\varepsilon(s)$ .

From the above discussion, the internal energy  $V$  can be described as follows:

$$V = U - \sum_i W_i. \quad (13)$$

Thus, the internal energy can also be represented in terms of the four variables,  $\phi(s)$ ,  $\theta(s)$ ,  $\psi(s)$ , and  $\varepsilon(s)$ .

### 3.2. Geometric Constraints

The interaction between the linear object and other objects such as fingertips or obstacles imposes geometric constraints on the linear object. Let us formulate these geometric constraints. The relative position between two points on the object is often controlled during a manipulative operation of the object. Consider a constraint that specifies the positional relationship between two points on the object. Let  $\mathbf{l} = [l_x, l_y, l_z]^T$  be a predetermined vector describing the relative position between two operational points,  $P(s_a)$  and  $P(s_b)$ . Recall that the spatial coordinates corresponding to distance  $s$  are given by eq. (6). Thus, the following equation must be satisfied:

$$\mathbf{x}(s_b) - \mathbf{x}(s_a) = \mathbf{l}. \quad (14)$$

The orientation at one point on the object is often controlled during an operation as well. This constraint is simply described as follows

$$A(\phi(s_c), \theta(s_c), \psi(s_c)) = A(\phi_c, \theta_c, \psi_c), \quad (15)$$

where  $\phi_c$ ,  $\theta_c$ , and  $\psi_c$  are predefined Eulerian angles at one operational point  $P(s_c)$ .

Contact between a linear object and rigid obstacles in operation space also yields other geometric constraints. Note that any point on the object must be located on or outside each obstacle. Let us describe the surface of an obstacle fixed in space by function  $f(\mathbf{x}) = 0$ . Assume that the value of the

function is positive inside the obstacle and negative outside it. The condition that a linear object is not interfered with by this obstacle is then described as follows

$$f(\mathbf{x}(s)) \leq 0, \quad \forall s \in [0, L], \quad (16)$$

where  $\mathbf{x}(s)$  is described in eq. (6). Note that the condition that an object is not interfered with by obstacles is described by a set of inequalities since mechanical contacts between the objects constrain the motion of the object unidirectionally.

Furthermore, self-interaction of a linear object should be considered. Assume that the cross-section of a linear object is circular. Let  $r(s)$  be the radius of the cross-section at point  $P(s)$ . Then, in order to avoid interference with itself, a linear object must satisfy the following condition:

$$\begin{aligned} |\mathbf{x}(s_i) - \mathbf{x}(s_j)| &\geq r(s_i) + r(s_j), \\ \forall s_i, s_j \in [0, L], \quad \text{s.t.} \quad |s_i - s_j| &\geq r(s_i) + r(s_j). \end{aligned} \quad (17)$$

From the above discussion, it is found that the geometric constraints imposed on a linear object are given by not only equational constraints such as eqs. (14) and (15) but also inequality constraints such as eqs. (16) and (17). The deformed shape of the object is, therefore, determined by minimizing the internal energy described in eq. (13) under these geometric constraints imposed on the object. Namely, computation of the deformed shape of an object results in a variational problem under equational and inequality constraints.

## 4. Computation of Linear Object Deformation

### 4.1. Computation Algorithm

Computation of the deformed shape of a linear object results in a variational problem as mentioned in the previous section. One method to solve a variational problem is the Euler approach, which is based on the stationary condition in function space. Recall that the geometric constraints resulting from mechanical contacts are unidirectional and mathematically describable by inequalities such as eqs. (16) and (17). These conditions are nonholonomic constraints (Goldstein 1980). Thus, the shape of an object that minimizes internal energy does not necessarily satisfy the stationary condition. This implies that the Euler approach, which is based on the stationary condition, is not applicable.

In this paper, we develop an algorithm based on the Ritz method (Elsigolc 1961) and a nonlinear programming technique. Let us express functions  $\phi(s)$ ,  $\theta(s)$ ,  $\psi(s)$ , and  $\varepsilon(s)$  by linear combinations of basic functions  $e_1(s)$ – $e_n(s)$ :

$$\begin{aligned} \phi(s) &= \sum_{i=1}^n a_i^\phi e_i(s) \triangleq \mathbf{a}^\phi \cdot \mathbf{e}(s), \\ \theta(s) &= \sum_{i=1}^n a_i^\theta e_i(s) \triangleq \mathbf{a}^\theta \cdot \mathbf{e}(s), \end{aligned}$$

$$\psi(s) = \sum_{i=1}^n a_i^\psi e_i(s) \triangleq \mathbf{a}^\psi \cdot \mathbf{e}(s),$$

$$\varepsilon(s) = \sum_{i=1}^n a_i^\varepsilon e_i(s) \triangleq \mathbf{a}^\varepsilon \cdot \mathbf{e}(s).$$

Here,  $\mathbf{a}^\phi$ ,  $\mathbf{a}^\theta$ ,  $\mathbf{a}^\psi$ , and  $\mathbf{a}^\varepsilon$  are vectors consisting of coefficients corresponding to functions  $\phi(s)$ ,  $\theta(s)$ ,  $\psi(s)$ , and  $\varepsilon(s)$ , respectively, and vector  $\mathbf{e}(s)$  is composed of basic functions  $e_1(s)$ – $e_n(s)$ . Substituting the above equations into eq. (13), internal energy  $V$  is described by a function of coefficient vectors  $\mathbf{a}^\phi$ ,  $\mathbf{a}^\theta$ ,  $\mathbf{a}^\psi$ , and  $\mathbf{a}^\varepsilon$ . The geometric constraints are also described by conditions involving the coefficient vectors. In addition, discretizing eqs. (16) and (17) by dividing interval  $[0, L]$  into  $N$  small intervals yields a finite number of conditions. As a result, a set of the geometric constraints is expressed by equations and inequalities in terms of the coefficient vectors.

Consequently, the deformed shape of a linear object can be derived by computing a set of coefficient vectors  $\mathbf{a}^\phi$ ,  $\mathbf{a}^\theta$ ,  $\mathbf{a}^\psi$ , and  $\mathbf{a}^\varepsilon$  that minimizes the internal energy under the geometric constraints. This minimization problem under equality and inequality constraints can be solved by the use of a non-linear programming technique such as the multiplier method (Avriel 1976). In this method, a minimization problem under geometric constraints is converted into an unconditional minimization problem with Lagrange multipliers. The Lagrange multipliers denote the components of reaction forces corresponding to individual geometric constraints. The shape of the deformed object corresponding to a set of coefficient vectors can be computed by eq. (6).

#### 4.2. Examples of Computation

In this section, numerical examples demonstrate how the proposed method computes the deformed shape of a linear object. The first example shows the transition between topologically different shapes of a linear object considering its flexural and torsional deformations. The second example demonstrates the effect of the extensional rigidity of a linear object on its shapes. The third example shows the shape of a linear object under gravity. The following set of basic functions are used in the computation of these examples:

$$e_1 = 1, \quad e_2 = s,$$

$$e_{2i+1} = \sin \frac{2\pi i s}{L},$$

$$e_{2i+2} = \cos \frac{2\pi i s}{L}, \quad (i = 1, 2, 3, 4).$$

Assume that the length of the object  $L$  is equal to 100 in the following examples. We apply the multiplier method and the BFGS formula in the quasi-Newton method to the non-linear optimization. The multiplier method converts a minimization problem with geometric constraints into an unconditional minimization problem. The BFGS formula solves the



Fig. 2. Computational result of topological shape transition.

converted unconditional minimization problem. All optimizations start from the natural state of a linear object. All the following computations were performed on a 833 MHz Alpha 21264 CPU with 1 GB memory operated by Tru64UNIX. Programs were compiled by a Compaq C Compiler V6.4 with optimization option -O4.

#### 4.3. Object Deformation Considering Flexure and Torsion

The first example demonstrates the deformation of a linear object with flexure and torsion. The potential energy of the object is assumed to be given by the sum of the flexural and torsional energies of the object:  $U = U_{flex} + U_{tor}$ . On normalizing the potential energy and the geometric constraints by dividing variable  $s$  by length  $L$ , it is found that the shape of the object is determined by the following dimensionless quantity:

$$\rho_t = \frac{R_t}{R_f}.$$

Suppose that  $\rho_t = 0.77$ . Let us align the central axis at both end points of a linear object in the initial state. Then, let us move one end point along this axis in order to shorten the distance between the two end points specified by  $l$ . Computed shapes of a linear object of length  $L$  are shown in Figure 2. Values of the distance  $l$  corresponding to the computed shapes are  $0.6L$ ,  $0.5L$ ,  $0.4L$ ,  $0.3L$ ,  $0.2L$ , and  $0.1L$ . The shape of a linear object changes from a knot-free shape into a one-knot shape while the distance between the two end points decreases, as shown in the figure. In a one-knot shape, the object has not only flexural deformation but also torsional deformation. Computation times are listed in Table 1. CPU time increases as length  $l$  decreases since optimization starts from the natural state of the linear object.

Figure 3 shows the computed flexural energy  $U_{flex}$  and the torsional energy  $U_{tor}$ . We have also plotted the flexural energy of a linear object with flexural deformation alone:  $U = U_{flex}$ . This figure shows that the sum of the flexural and torsional energies is smaller than the flexural energy without torsional

**Table 1. Time to Compute Topologically Different Shapes**

$l$	$0.6L$	$0.5L$	$0.4L$	$0.3L$	$0.2L$	$0.1L$
CPU time (s)	17.6	23.1	26.5	35.5	38.6	38.5

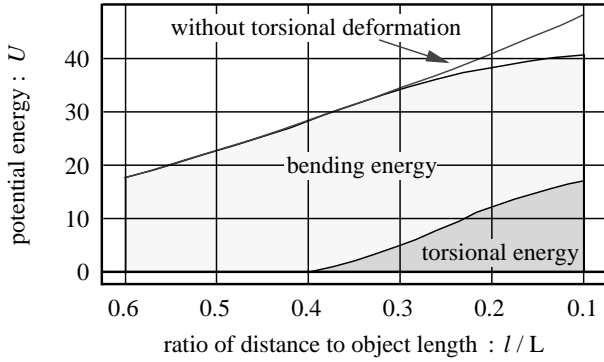


Fig. 3. Potential energy in topological shape transition.

deformation when the ratio  $l/L$  is below a boundary value, 0.3 in this example. The deformed shape transits between a knot-free shape and a one-knot shape at the boundary value. We also found that the boundary value, which can be determined through the above computation, depends on  $\rho_e$ . As a result, a linear object changes from a knot-free shape into a one-knot shape as the ratio  $l/L$  drops below a boundary value, which depends on the flexural and torsional rigidities. As demonstrated here, our proposed approach can simulate this topological shape transition.

Kinking, or torsional buckling, is a well-known phenomenon in linear object deformation including flexure and torsion. Our proposed approach is capable of simulating this phenomenon. Figure 4 shows the result of computed kinking. Let us first twist a linear object, i.e., fix one end point of the object and rotate the other around its central axis. Then, let us reduce the distance between the two end points. Let  $\omega_0$  be the twisting angle. The left two shapes in the figure correspond to the twisting phase at  $\omega_0 = 2\pi$  and  $4\pi$ . The other four shapes in the figure correspond to the reducing phase at  $l = 0.8L, 0.6L, 0.4L,$  and  $0.2L$ . A knot is formed in the object at any value of distance  $l$ , as shown in the figure. Recall that a linear object has no knots when  $l/L$  exceeds 0.3 without initial twisting. This example demonstrates how a knot is generated with the initial twisting. Computation times are listed in Table 2. CPU time increases with twisting angle  $\omega_0$  since optimization starts from the natural state of a linear object. Figure 5 shows the flexural and torsional energies during a kinking process. Twisting of a linear object increases the energy of the object and reducing the distance between the end points decreases the energy, as shown in the figure.



Fig. 4. Computational result of kinking.

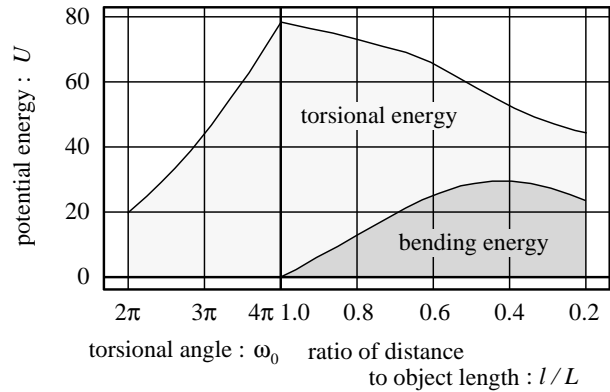


Fig. 5. Potential energy in kinking.

**4.4. Effect of Object Extension**

The second example demonstrates the computation of the object shape considering the extensional energy. The potential energy of a linear object is given by the sum of its flexural and extensional energies:  $U = U_{flex} + U_{ext}$ . On normalizing as in the first example, it is found that the shape of the object is determined by the following dimensionless quantity:

$$\rho_e = \frac{R_e}{R_f} L^2.$$

**Table 2. Time to Compute Deformation in Kinking**

$\omega_0$	$2\pi$	$3\pi$	$4\pi$	$l$	$0.8L$	$0.6L$	$0.4L$	$0.2L$
CPU time (s)	8.5	17.2	29.6	CPU time (s)	30.5	32.6	30.0	35.0

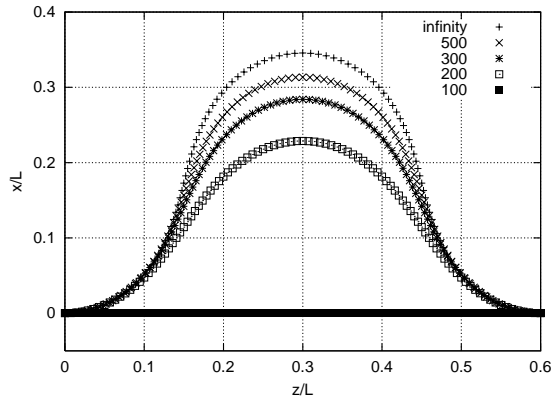


Fig. 6. Example of computed object shapes considering extension.

Quantity  $\rho_e$  represents the contribution of the extensional energy to the shape of a linear object. The extension is small when the quantity  $\rho_e$  is large and it is nil at  $\rho_e = \infty$ . Let us compute the deformed shapes of a linear object at  $\rho_e = \infty, 500, 300, 200,$  and  $100$ . The distance between the end points along the  $z$ -axis is set to  $0.6L$  in this computation. The computed shapes are shown in Figure 6. Note that the length of the object is less than the original length  $L$ . The height and length of the object decrease with decreasing  $\rho_e$ , as shown in the figure. Extensional deformation without flexural deformation occurs when parameter  $\rho_e$  is less than 100.

**4.5. Effect of Gravity**

The third example demonstrates the computation of the object shape considering the gravitational energy. The potential energy of a linear object is then given by the sum of its flexural and gravitational energies:  $U = U_{flex} + U_{grav}$ . On normalizing as in the first example, it is found that the shape of the object is determined by the following dimensionless quantity:

$$\rho_g = \frac{D}{R_f} L^3.$$

Quantity  $\rho_g$  represents the contribution of the gravitational energy to the shape of a linear object. The gravitational effect is negligible at  $\rho_g = 0$ . Let us compute the deformed shapes of a linear object at  $\rho_g = 0, 100, 150, 200,$  and  $400$ . The distance between the end points along the  $z$ -axis is taken to be  $0.85L$  in

this computation. The computed shapes are shown in Figure 7. As shown in the figure, the height of the object decreases with increasing  $\rho_g$ . In addition, the shape is no longer symmetric when  $\rho_g$  exceeds 100. Note that we have two possible shapes that are mirror images about the central vertical line. One of the shapes is illustrated in the figure. In order to verify that the asymmetric shape minimizes the potential energy, let us compute the potential energy of the object assuming that the deformed shape is symmetric. The potential energy  $U$  is, for example, equal to 0.255 assuming that the deformed shape is symmetric while the minimum value of potential energy is equal to 0.254 at  $\rho_g = 200$  resulting from  $R_f = 1, D = 2 \times 10^{-4}$ , and  $L = 100$ . That is, the symmetric shape does not satisfy the condition that the potential energy is at its minimum in a stable deformed shape. This implies that deformed shapes are asymmetric when the dimensionless quantity  $\rho_g$  exceeds a certain value.

**5. Experimental Verification**

**5.1. Two-Dimensional Shape Measurement**

In this section, the computation results will be experimentally verified by measuring the deformed shape of a linear object. Let us measure the 2D deformation of two types of paper sheets as shown in Figure 8. One is a rectangle 30 mm wide, and the other is a trapezoid whose upper and lower bases are 50 and 100 mm wide, respectively. Both are 200 mm long and 92  $\mu$ m thick. Let us evaluate the deformed shape of a paper illustrated in Figure 8(a) along the  $z$ - $x$  plane. The flexural rigidity  $R_f$  and the weight  $D$  per unit length of the paper are  $9.8 \times 10^{-5} \text{ N m}^2$  and  $2.0 \times 10^{-2} \text{ N m}^{-1}$ , respectively. The paper is deformed so that the distance between its ends is 180, 140, or 70 mm. Quantity  $\rho_g$  turns out to be equal to 1.60. This implies that the gravitational energy is negligible in the computation. Angles  $\theta(0)$  and  $\theta(L)$  are measured and are estimated as 0.17 and 0 (rad), respectively. The computed and measured shapes of the deformed paper are shown in Figure 9 as solid and dotted lines, respectively. The difference between the computed and experimental values along the  $z$ -axis is 2 mm at most. Namely, the ratio of the difference in paper length is approximately 1%.

Next, let us evaluate the deformed shape of a paper illustrated in Figure 8(b). The flexural rigidity  $R_f$  and the weight  $D$  per unit length change according to the paper width  $b$  mm and are taken to be  $3.23b \times 10^{-6} \text{ N m}^2$  and  $6.86b \times 10^{-4} \text{ N m}^{-1}$ , respectively. Furthermore, the width  $b$  is given by  $50 + 0.25s$  mm. Note that our approach can be

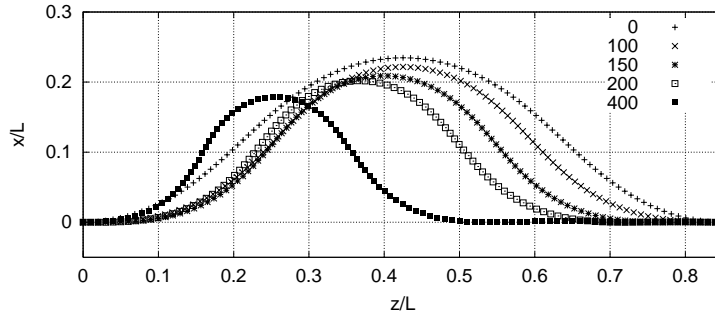


Fig. 7. Example of computed object shapes considering gravity.

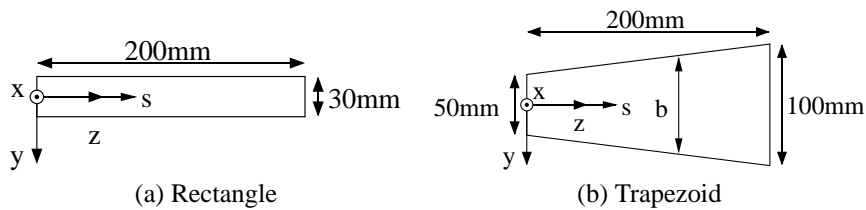


Fig. 8. Shape of papers used in experiment.

applied to the deformation of a linear object when its physical properties depend on variable  $s$ . Angles  $\theta(0)$  and  $\theta(L)$  are estimated as 0.17 and 0 (rad), respectively. The computed and measured shapes of the deformed paper are illustrated in Figure 10. The difference between the computed and experimental values along the  $z$ -axis is 2 mm at most. Namely, the ratio of the difference in the paper length is approximately 1%.

Let us verify asymmetric deformation plotted in Figure 7. We have measured the deformation of rectangular papers 15 mm wide and 60  $\mu\text{m}$  thick. The flexural rigidity  $R_f$  and the weight  $D$  per unit length of the papers are  $1.4 \times 10^{-6} \text{ N m}^2$  and  $8.8 \times 10^{-3} \text{ N m}^{-1}$ . The length of the papers  $L$  is taken to be 200, 300, and 400 mm. Then, quantity  $\rho_g$  is correspondingly given by 50, 172, and 405. The papers are deformed so that the distance between the end points is  $0.85L$ . The measured shapes are plotted in Figure 11. Comparing Figures 11 and 7, we find that the computation describes the measured asymmetric deformation well. The maximum difference between the computed and experimental values along the  $z$ -axis is 7 mm at  $L = 200$  mm, 20 mm at  $L = 300$  mm, and 20 mm at  $L = 400$  mm. Thus, the ratio of the difference in paper length is approximately 4% at  $L = 200$  mm, 7% at  $L = 300$  mm, and 5% at  $L = 400$  mm. The difference in the last experiment is larger than that in the first two experiments. The deformed shapes are almost entirely determined by the orientation angle at each end point and the flexural rigidity in the first two ex-

periments since the gravitational energy is negligible, while, in the last experiment, the weight per unit length plays a role as well. In other words, more parameters must be determined in the last experiment than in the first two. This is what causes the larger difference in the last experiment.

### 5.2. Three-Dimensional Shape Measurement

In this section, we describe the measurement of 3D deformation of a linear object. We have measured the shape of a metal wire 871 mm long. The wire's flexural rigidity  $R_f$  and the torsional rigidity  $R_t$  are  $6.6 \times 10^{-4} \text{ N m}^2$  and  $2.3 \times 10^{-4} \text{ N m}^2$ , respectively. Weight  $D$  per unit length of the wire is  $1.0 \times 10^{-2} \text{ N m}^{-1}$ . Two manipulators control the position and orientation of both end points of the wire. In the initial state, one end point is rotated by  $\omega_0$  while keeping the wire straight. Next, the distance between the two end points  $l_z$  is decreased by controlling the motion of the two manipulators. Then, the object is both flexed and twisted. This implies that its shape is no longer limited to one plane. The shape of the deformed wire is measured by two cameras. The optical axes of the cameras intersect at one point at right angles. Let one optical axis be the  $x$ -axis and the other axis be the  $y$ -axis. The projections of the deformed shape onto the  $z$ - $x$  and  $z$ - $y$  planes can then be directly measured by the two cameras.

Figure 12 shows the computed and measured shapes of a deformed wire at  $\omega_0 = \pi$  (rad). The solid and dotted lines represent the computed and measured values, respectively. From

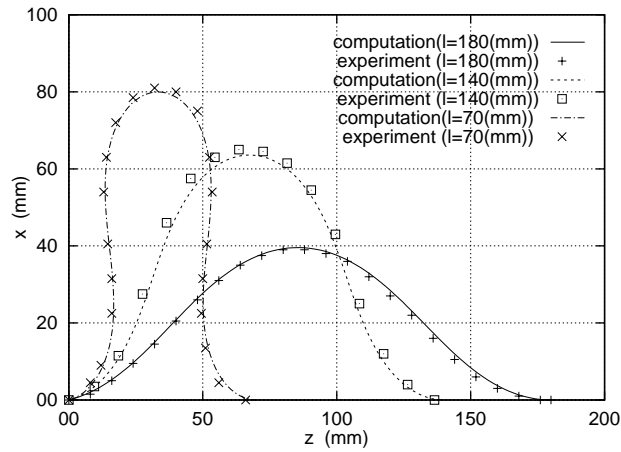


Fig. 9. Computed and measured shapes of rectangular paper.

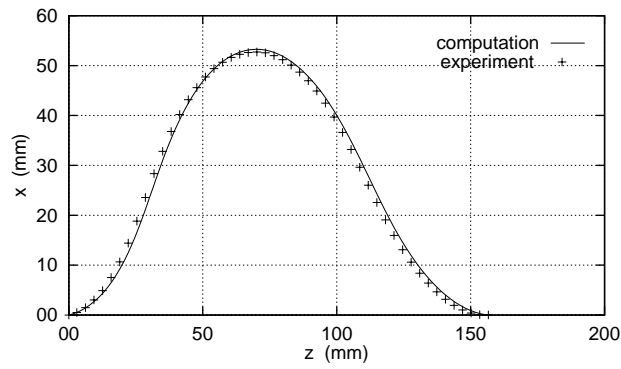


Fig. 10. Computed and measured shapes of trapezoidal paper.

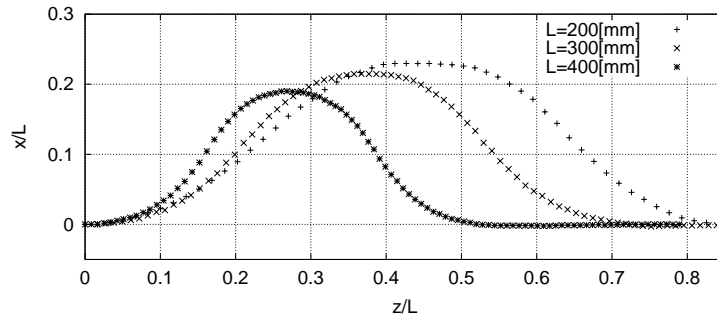


Fig. 11. Measured asymmetric deformation of symmetric paper.

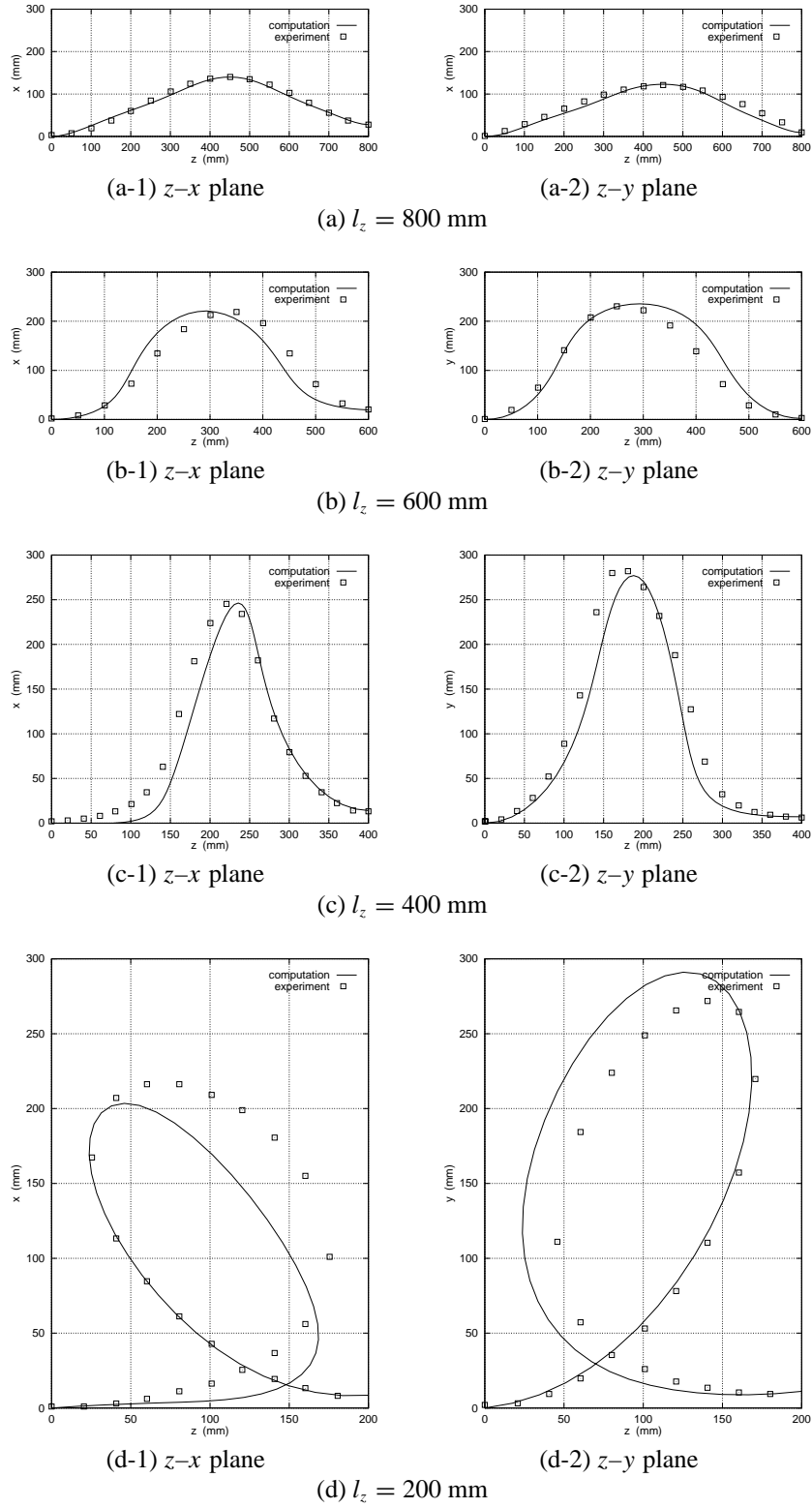


Fig. 12. Computed and measured 3D shapes of wire.

the measured values, the distances between the two end points along the  $x$ -axis and  $y$ -axis,  $l_x$  and  $l_y$ , and the orientations at the end points,  $A(\phi(0), \theta(0), \psi(0))$  and  $A(\phi(L), \theta(L), \psi(L))$ , have been estimated. The estimated values have been used in the computation of the deformed shapes of a wire. The gravitational effect is assumed to be negligible. The difference between the computed and experimental values along the  $x$ - and  $y$ -axes is 50 mm at most. The ratio of the difference in the wire length is approximately 6%. The difference in this 3D experiment is larger than the difference in the first two 2D experiments. Note that more parameters must be determined in the 3D experiment: three orientation angles at each end point of the wire and its torsional rigidity. This causes the larger difference in the 3D experiment.

## 6. Grasping of Deformable Linear Object

### 6.1. Stability of Deformable Object Grasping

In this section, we apply the proposed approach to the grasping of a deformable linear object. Force closure has been proposed to evaluate the stability of the grasping of a rigid object (Mason 2001). The stability is examined by investigating whether force/moment equilibrium is kept or is broken against an arbitrary disturbance force/moment applied to the object. Note that a set of forces applied to a rigid object at different points can be equivalently converted into a combination of force and moment at one representative point. This conversion originates from the definition of a rigid body: the distance between any two points on the object is invariant. On the other hand, the conversion cannot be performed for a set of forces applied to a deformable object since the distance between two points on the object may vary. Moreover, in the grasping of a rigid object, it is often assumed that each finger can exert a grasping force involved in the friction cone at the contacting point with infinite magnitude. This assumption is not applicable to the grasping of a deformable linear object since the magnitude of the grasping forces can be determined depending on the deformed shape of the linear object.

Let us evaluate the stability of the grasping of a deformable linear object. The above discussion suggests that a disturbance force should be applied to different points on the object to investigate whether the grasping can be performed successfully against the disturbance force. Note that applying a disturbance force to a deformable linear object causes deformation, which may break the contact between the object and a finger, resulting in failure of the grasp. The breakage depends on the magnitude of the disturbance force as well as its direction and action point. We can examine if the grasping can be performed successfully by investigating whether or not the grasping forces are involved in their corresponding friction cones.

Let us formulate the above discussion on the grasping of a deformable linear object. Assume that a deformable linear

object contacts with  $n$  fingers. Let  $P(s_k)$  be the contacting point between the  $k$ th finger and the object, let  $\mathbf{f}_k$  be the contacting force of the finger, and let  $FC_k$  be the friction cone at the contacting point. Let  $f$  and  $\mathbf{n}$  be the magnitude and direction, respectively, of a disturbance force applied to a point  $P(s_a)$  on the object. Let us apply a disturbance force  $f\mathbf{n}$  at point  $P(s_a)$ . Unless the magnitude of the disturbance force exceeds a certain upper bound, the contacts at individual fingers are kept and all contacting forces are involved in their corresponding friction cones. In other words, the grasping can be performed successfully against the disturbance force while its magnitude is below the bound. Note that the upper bound depends on direction  $\mathbf{n}$  and position  $\mathbf{x}(s_a)$  of point  $P(s_a)$ . Let  $F(s_a, \mathbf{n})$  be the upper bound of magnitude  $f$ . If the magnitude exceeds the bound, contact at a finger is lost, resulting in failure of the grasp. Let  $F_{mub}$  be the smallest value of  $F(s_a, \mathbf{n})$ :

$$F_{mub} = \min_{s_a} \min_{\mathbf{n}} F(s_a, \mathbf{n}).$$

Note that the grasping can be performed successfully unless the magnitude of a disturbance force exceeds  $F_{mub}$ , regardless of the direction of the force and its action point. That is,

$$\forall f \in [0, F_{mub}], \forall \mathbf{n} \text{ s.t. } \|\mathbf{n}\| = 1,$$

$$\forall s_a \text{ s.t. } 0 \leq s_a \leq L,$$

$$\exists \mathbf{f}_1 \in FC_1, \dots, \mathbf{f}_k \in FC_k, \text{ s.t.}$$

a linear object is stable against external force  $f\mathbf{n}$  applied to the object at  $\mathbf{x}(s_a)$ .

The value of  $F_{mub}$ , which is referred to as the disturbance force margin, indicates the stability of the grasping of a deformable linear object.

### 6.2. Numerical Example of Grasping Evaluation

Let us demonstrate how to compute the disturbance force margin by taking a simple example of 2D grasping of a deformable linear object. Assume that a linear object is 100 units long and 0.1 units thick. Its flexural rigidity is assumed to be 1. Let us evaluate the stability of the two grasplings illustrated in Figure 13. In Figure 13(a), two fingers push a linear object at both end points of the object. The object can rotate around the end points. Let  $l$  be the distance between the two end points of the object. Let the left end point of the initial shape be the origin of the space coordinate system. The fingers impose the following geometric constraints on the object:

$$\text{left finger: } z(0) \geq 0, \quad x(0) = 0,$$

$$\text{right finger: } z(L) \leq l, \quad x(L) = 0.$$

Note that inequality  $z(0) > 0$  implies that the contact at the left end point is lost and inequality  $z(L) < l$  shows that the contact at the right end point is also lost. Components of a grasping force correspond to the Lagrange multipliers for the

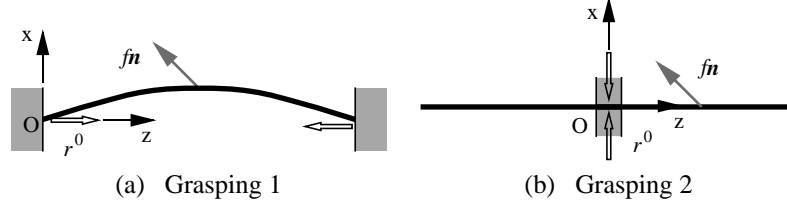


Fig. 13. Two grasplings of a deformable linear object.

above geometric constraints. Note that, when  $z(0) > 0$  is satisfied, the corresponding Lagrange multiplier is equal to zero, which implies that the  $z$ -component of the contact force at the left end point vanishes. When  $z(L) < l$  is satisfied, the corresponding Lagrange multiplier is equal to zero, so that the  $z$ -component of the grasping force at the right end point vanishes. Let  $\mu$  be the coefficient of friction between the object and the fingers. Friction cones at the end points are described as follows:

$$\begin{aligned} \text{FC}_1 &= \left\{ \begin{array}{l} \left[ \begin{array}{l} cf_z \\ f_x \end{array} \right] \\ -\mu f_z - f_x \leq 0, \quad -\mu f_z + f_x \leq 0 \end{array} \right\}, \\ \text{FC}_2 &= \left\{ \begin{array}{l} \left[ \begin{array}{l} cf_z \\ f_x \end{array} \right] \\ \mu f_z - f_x \leq 0, \quad \mu f_z + f_x \leq 0 \end{array} \right\}. \end{aligned}$$

Thus, whether each grasping force is involved in the corresponding friction cone can be examined by evaluating two inequalities. Consequently, it can be investigated whether the grasping is performed successfully or not. In Figure 13(b), a pair of two fingers pinches a linear object at its center. Let the center point of the initial shape be the origin of the space coordinate system. The fingers impose the following geometric constraints on the object:

$$\begin{aligned} \text{top finger:} \quad & z(L/2) = 0, \quad x(L/2) \leq 0, \\ \text{bottom finger:} \quad & z(L/2) = 0, \quad x(L/2) \geq 0. \end{aligned}$$

We can then determine whether or not the grasping is performed successfully by the above procedure.

When a disturbance force is imposed on a linear object at point  $P(s_a)$ , the curvature may change discontinuously at this point. This implies that not all differential geometry coordinates can be approximated by a linear combination of continuous basic functions. Thus, each differential geometry coordinate will be approximated by two combinations. That is, two coefficient vectors will be introduced to approximate each coordinate. For example, coordinate  $\theta(s)$  is approximated as follows:

$$\theta(s) = \begin{cases} \mathbf{a}_l^\theta \cdot \mathbf{e}(s) & (s \leq s_a) \\ \mathbf{a}_r^\theta \cdot \mathbf{e}(s) & (s \geq s_a) \end{cases}$$

where

$$\theta(s_a) = \mathbf{a}_l^\theta \cdot \mathbf{e}(s_a) = \mathbf{a}_r^\theta \cdot \mathbf{e}(s_a).$$

This equation imposes a continuity condition on coordinate  $\theta(s)$ . Let  $\mathbf{a}_l$  and  $\mathbf{a}_r$  be collective vectors consisting of coefficient vectors corresponding to the left and right parts, respectively. Potential energy is the sum of the energy of the left part, which is described by  $\mathbf{a}_l$ , and the energy of the right part, which is described by  $\mathbf{a}_r$ . For example,

$$U_{flex}(\mathbf{a}_l, \mathbf{a}_r) = \frac{1}{2} \int_0^{s_a} R_f \kappa^2(\mathbf{a}_l) ds + \frac{1}{2} \int_{s_a}^L R_f \kappa^2(\mathbf{a}_r) ds.$$

Work done by a disturbance force is formulated as follows

$$W = \mathbf{f}_{dist} \cdot \{\mathbf{x}(s_a) - \mathbf{x}_0(s_a)\}$$

where  $\mathbf{f}_{dist}$  denotes the disturbance force at point  $P(s_a)$  and  $\mathbf{x}_0(s_a)$  is the initial position of the point. Potential energy  $U$  and work  $W$  are included in eq. (13). The deformed shape can be computed by solving a constrained optimization problem with respect to the collective vectors  $\mathbf{a}_l$  and  $\mathbf{a}_r$  under continuity conditions of differential geometry coordinates at point  $P(s_a)$ .

Let us compute the stability of the two grasplings illustrated in Figure 13. We will evaluate the first grasping at  $l = 0.95L$ ,  $0.80L$ , and  $0.60L$ . The magnitude of the initial grasping force is correspondingly given by  $r^0 = 1.02 \times 10^{-3}$ ,  $1.10 \times 10^{-3}$ , and  $1.24 \times 10^{-3}$ . We will evaluate the second grasping at the same values of the magnitude  $r^0 = 1.02 \times 10^{-3}$ ,  $1.10 \times 10^{-3}$ , and  $1.24 \times 10^{-3}$ . Figure 14 illustrates the shape of a linear object deformed by a disturbance force. It takes, on average, 25 s to compute one of the deformed shapes shown in the figure. Figure 14(a) corresponds to the first grasping at  $r^0 = 1.10 \times 10^{-3}$ . A disturbance force with  $s_a = 0.5L$  and  $\mathbf{n} = [-1/\sqrt{2}, 1/\sqrt{2}]^T$  is applied to the object. Let us compute the deformed shapes when  $f = 0.0 \times 10^{-3}$ ,  $1.4 \times 10^{-3}$ ,  $1.7 \times 10^{-3}$ , and  $2.0 \times 10^{-3}$ . As shown in the figure, contact at the right end point is lost when the magnitude of the disturbance force exceeds  $1.4 \times 10^{-3}$ . Figure 14(b) corresponds to the second grasp at  $r^0 = 1.10 \times 10^{-3}$ . A disturbance force with  $s_a = 0.75L$  and  $\mathbf{n} = [-1/\sqrt{2}, 1/\sqrt{2}]^T$  is applied to the object. Contact between the object and the fingers is maintained even if the magnitude of the disturbance force reaches  $2.0 \times 10^{-3}$ . In this grasping, a deformed shape maintains contact at all grasping points for any magnitude of the disturbance force.

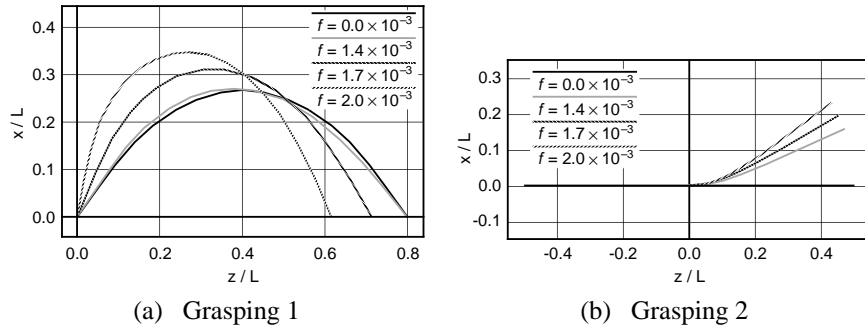


Fig. 14. Object shapes deformed by disturbance force.

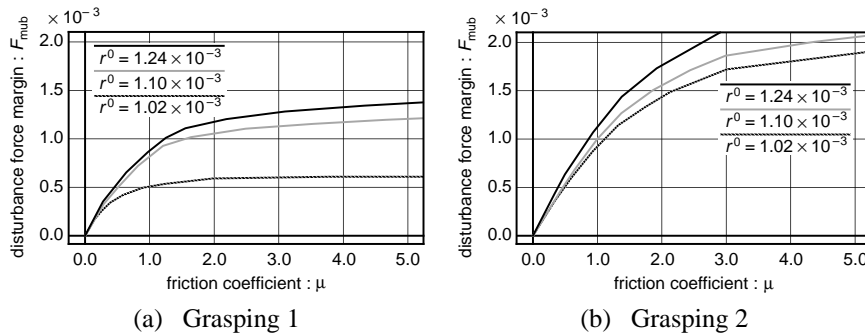


Fig. 15. Relationship between disturbance force margin and friction coefficient.

This implies that the normal reaction force at each point is positive but does not imply that the tangential force lies within the maximum friction force.

After computing the deformed shape and contact forces at grasping points, we can compute the disturbance force margin by examining if each computed contact force is involved in the friction cone at each point. Figure 15 shows the relationship between the disturbance force margin  $F_{mub}$  and the coefficient of friction  $\mu$ . We have applied disturbance forces of three different magnitudes, at nine action points, and in nine directions to obtain the relationship at each grasping. This means that it takes about 100 minutes to plot each graph in the figure. The figure shows that the second grasping is more stable than the first grasping. Furthermore, larger values of friction coefficient  $\mu$  and initial grasping force  $r^0$  increase the stability in each grasping.

## 7. Deformation Path Planning in Linear Object Manipulation

### 7.1. Description of Deformation Path

In the manipulation of a deformable linear object, the object is often deformed from one shape into another. Let us determine an appropriate deformation path from an initial shape to a goal

shape. It is generally required to deform a linear object with little damage to the object. Excessive potential energy of a linear object can be easily transformed into kinetic energy by a small disturbance force, in which case the shape of the object may become unstable and change dynamically. Thus, the potential energy of a linear object should be small during its deformation process. It is found that a deformation path that minimizes the value of the potential energy maximum is preferable.

Recall that the deformation of a linear object can be described by coefficient vectors corresponding to Eulerian angles and extensional strain. Let  $\mathbf{a}$  be a collective vector of these coefficients. One deformation corresponds to a point in coefficient space. The deformation process of a linear object is then given by a path in the coefficient space. Let  $\mathbf{a}_0$  and  $\mathbf{a}_1$  be the initial and goal deformations, respectively, and let  $\mathbf{a}(k)$  ( $0 \leq k \leq 1$ ) be a path from the initial deformation to the goal deformation. Note that functions  $1 - k$ ,  $k$ , and  $k^i(1 - k)$  ( $i = 1, 2, \dots$ ) are a set of bases of a function space. Then, any path can be approximated by a linear combination of these basic functions

$$\mathbf{a}(c, k) = (1 - k)\mathbf{a}_0 + k\mathbf{a}_1 + \sum_{i=1}^{\infty} c_i k^i (1 - k)$$

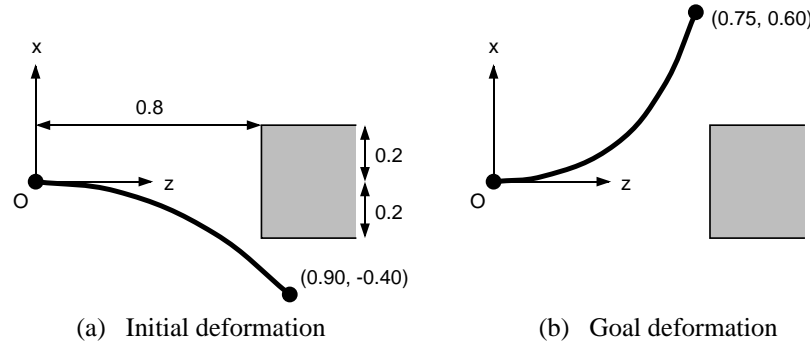


Fig. 16. Example of planar operation of linear object.

where  $\mathbf{c}_1$ – $\mathbf{c}_\infty$  are expansion coefficients. Any path can be represented by an infinite number of coefficient vectors:  $\mathbf{c}_1$ – $\mathbf{c}_\infty$ . Let  $\mathbf{c}$  be a collective vector consisting of these coefficient vectors, which is referred to as the deformation path vector. The deformation path vector  $\mathbf{c}$  determines a deformation path from the initial deformation  $\mathbf{a}(\mathbf{c}, 0) = \mathbf{a}_0$  to the goal deformation  $\mathbf{a}(\mathbf{c}, 1) = \mathbf{a}_1$ . Vector  $\mathbf{a}(\mathbf{c}, k)$  corresponds to an intermediate deformation along the path.

Let  $U(\mathbf{c}, k)$  be the potential energy of a linear object with deformation  $\mathbf{a}(\mathbf{c}, k)$ . Let  $U_{max}(\mathbf{c})$  be the maximum of the potential energy along a deformation path represented by  $\mathbf{c}$ :

$$U_{max}(\mathbf{c}) = \max_{0 \leq k \leq 1} U(\mathbf{c}, k).$$

Recall that geometric constraints imposed on an object can be described by a set of functions of vector  $\mathbf{c}$ . Consequently, it is found that the optimal deformation path can be derived by minimizing the function  $U_{max}(\mathbf{c})$  under the geometric constraints.

## 7.2. Example of Deformation Path Planning

Let us show a numerical example in order to demonstrate how the deformation path is computed by our approach. Figure 16 shows an example of a planar operation. The initial deformation of a linear object is shown in Figure 16(a) and its goal deformation is given in Figure 16(b). In this example, it is assumed that a linear object has no torsional deformation and that its gravitational energy is negligible. Namely, the potential energy consists of flexural energy alone:  $U = U_{flex}$ . In other words, angles  $\phi$  and  $\psi$  are constantly zero, implying that the linear object is deformed in a plane.

The angle of the left end point of the object is fixed. The object must avoid an obstacle illustrated in the figure. Thus, geometric constraints imposed on the object are represented as follows:

$$\begin{aligned} \theta(0, k) &= 0, \quad \forall k \in [0, 1], \\ z(s, k) &\leq 0.8, \quad \forall \{s \mid -0.2 \leq x(s, k) \leq 0.2\}, \\ &\forall k \in [0, 1]. \end{aligned}$$

Let us approximate a deformation path by the first five terms:

$$\mathbf{a}(\mathbf{c}, k) = (1 - k)\mathbf{a}_0 + k\mathbf{a}_1 + \sum_{i=1}^3 \mathbf{c}_i k^i (1 - k).$$

The deformation path vector  $\mathbf{c}$  then consists of a finite number of vectors:  $\mathbf{c}_1$ ,  $\mathbf{c}_2$ , and  $\mathbf{c}_3$ . Figure 17 shows the computed optimal deformation path. It takes 8 s to compute the optimal deformation path shown in the figure. The right side of the object is first guided downward from the initial location, then moved upward, and finally moved downward to the goal location. The position and orientation of the right end point are plotted in Figure 18.

Let us verify if the optimal deformation path can be performed by controlling the position and orientation of the right end point of a linear object. Thus, let us compute a deformation path of a linear object when the position and orientation of its right end point are given as plotted in Figure 18. This path is referred to as a feasible deformation path. The optimal and feasible deformation paths are plotted in Figure 19. The two paths coincide with each other well. Namely, this optimal path can be performed by controlling the location of the right end point alone in this example. The experimental result is also plotted in the figure. The deformation of a sheet of vinyl chloride 100 mm long, 12 mm wide, and 0.5 mm thick has been measured. The experimental result agreed well with the computed feasible deformation path. In this example, the optimal path was performed by controlling the location of the right end point of the object.

Generally, the optimal path may not be performed by controlling one end point of a linear object. A set of control points may be needed to perform the optimal path within a given

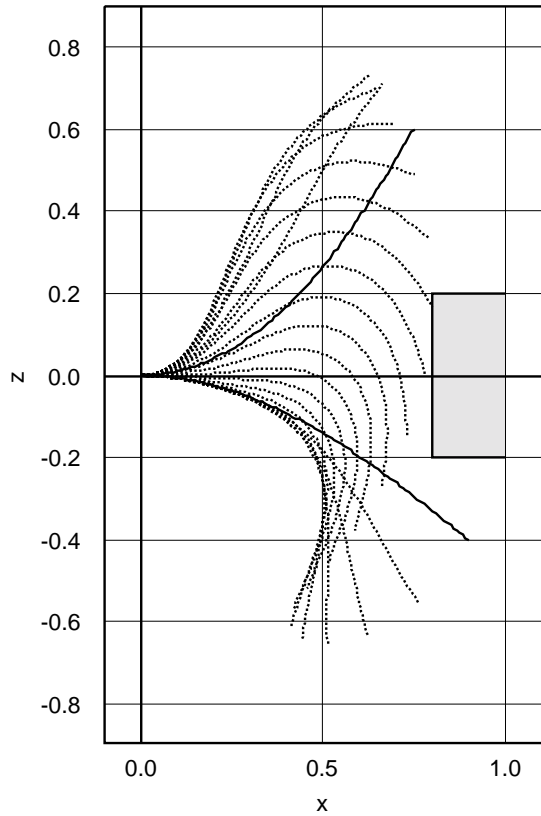


Fig. 17. Computed optimal deformation path.

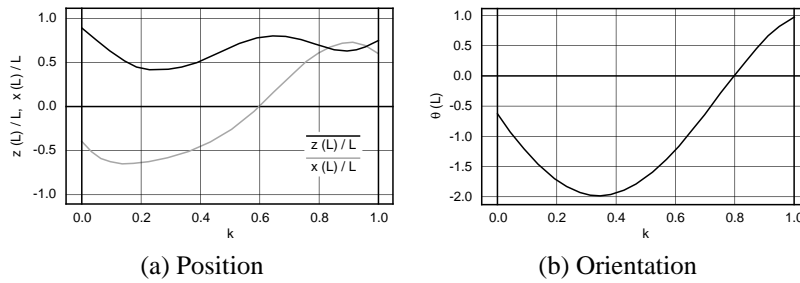


Fig. 18. Motion of right end point in optimal deformation path.

approximation. Feasibility can be examined by simulating a deformation path performed by the set of control points.

### 8. Concluding Remarks

We have described a modeling approach for linear object deformation based on an extension of differential geometry and its applications to grasping and deformation path planning. First, we reformulated the description of linear object de-

mation within the context of differential geometry to obtain a clearer mathematical expression. We redefined curvature and torsional angle so that any expression of the rotation matrix could be applied to the reformulated description. Secondly, we have presented deformation computations for linear objects to demonstrate the feasibility of the proposed modeling approach. We have shown that the developed model can simulate kinking and asymmetric deformation under gravity. One drawback of the proposed model is the relatively long computation time: 10–40 s per deformation. This was caused by

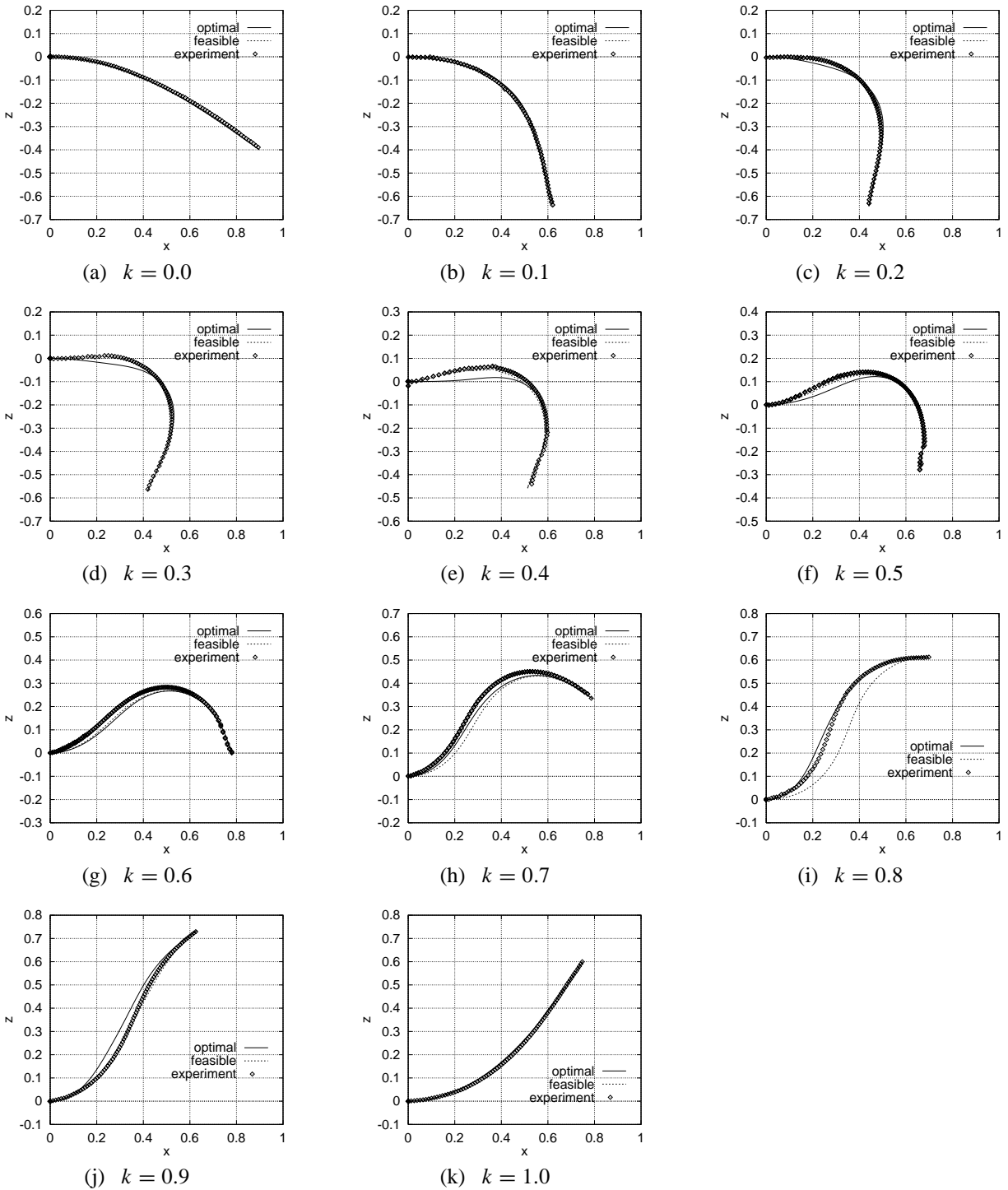


Fig. 19. Optimal deformation path, feasible deformation path, and experimental result.

the optimization calculus, which is essential in energy-based static modeling. Next, we compared computational and experimental results. We have found that the difference was 1% in 2D deformation if the gravity is negligible while it went up to 7% otherwise, and it exceeded 6% in 3D deformation. This difference may be due to the discrepancy of parameters including rigidities and orientation angles at either end point. Finally, we demonstrated that the proposed method can be employed for manipulative operations of deformable linear objects, such as grasping and deformation path evaluation. We have proposed the disturbance force margin to evaluate the stability of the grasping. The proposed method has been successfully applied to the computation of the margin. Also, it has been successfully applied to computation of the optimal deformation path.

The proposed approach is applicable to manipulative operations of a linear object including its self-interference. Thus, we will use it to describe knotting and raveling manipulation of a linear object. Identification of physical parameters and boundary conditions at operational points presents a challenge which, if met, would improve the model accuracy. In this paper, we have developed static modeling of linear object deformation. Future research will include a study on dynamic modeling of linear object deformation based on differential geometry.

## References

- Adams, C. C. 1994. *The Knot Book: An Elementary Introduction to the Mathematical Theory of Knots*, Henry Holt & Co., New York.
- Avriel, M. 1976. *Nonlinear Programming: Analysis and Methods*, Prentice-Hall, Englewood Cliffs, NJ.
- Baraff, D. and Witkin, A. 1998. Large steps in cloth simulation. In *Computer Graphics Proceedings (SIGGRAPH 1998)*, Orlando, FL, pp. 43–54.
- Belytschko, T., Liu, W. K., and Moran, B. 2000. Beams and shells. In *Nonlinear Finite Elements for Continua and Structures*, Chap. 9, Wiley, New York, pp. 509–568.
- Chen, M. Z. and Zheng, Y. F. 1995. Vibration-free handling of deformable beams by robot end-effectors. *Journal of Robotic Systems* 12(5):331–347.
- Daldegan, A., Thalmann, N. M., Kurihara, T., and Thalmann, D. 1993. An Integrated System for Modeling, Animating and Rendering Hair. *Computer Graphics Forum (Eurographics '93)*, 12(3):211–221.
- Debunne, G., Desbrun, M., Cani, M.-P., and Barr, A. H. 2001. Dynamic real-time deformations using space and time adaptive sampling. In *Computer Graphics Proceedings (SIGGRAPH 2001)*, Los Angeles, CA, pp. 31–36.
- Eberhardt, B., Weber, A., and Strasswer, W. 1996. A fast, flexible, particle-system model for cloth draping. *IEEE Computer Graphics and Applications*, 16(5):52–59.
- Eischen, J. W., Deng, S., and Clapp, T. G. 1996. Finite-element modeling and control of flexible fabric parts. *IEEE Computer Graphics and Applications*, 16(5):71–80.
- Elsgolc, L. E. 1961. *Calculus of Variations*, Pergamon, Oxford.
- Fung, Y. C. 1965. *Foundations of Solid Mechanics*, Prentice-Hall, Englewood Cliffs, NJ.
- Goldstein, H. 1980. *Classical Mechanics*, Addison-Wesley, Reading, MA.
- Gray, A. 1993. *Modern Differential Geometry of Curves and Surfaces*, CRC Press, Boca Raton, FL.
- Henrich, D. and Wörn, H. editors. 2000. *Robot Manipulation of Deformable Objects*, Advanced Manufacturing Series, Springer-Verlag, Berlin.
- Hirai, S. 2000. Energy-based modeling of deformable linear objects. In *Robot Manipulation of Deformable Objects*, D. Henrich and H. Wörn, editors, Advanced Manufacturing Series, Springer-Verlag, Berlin, pp. 11–28.
- Hirai, S. and Wada, T. 2000. Indirect simultaneous positioning of deformable objects with multi pinching fingers based on uncertain model. *Robotica*, Millennium Issue on Grasping and Manipulation, 18:3–11.
- Hopcroft, J. E., Kearney, J. K., and Krafft, D. B. 1991. A case study of flexible object manipulation. *International Journal of Robotics Research* 10(1):41–50.
- Irvine, H. M. 1981. *Cable Structures*, MIT Press, Cambridge, MA.
- James, D. L. and Pai, D. K. 1999. ArtDefo—accurate real time deformable objects. In *Computer Graphics Proceedings (SIGGRAPH 1999)*, Los Angeles, CA, pp. 65–72.
- James, D. L. and Pai, D. K. 2002. Real-time simulation of multizone elastokinematic models. In *Proceedings of the IEEE International Conference on Robotics and Automation*, Washington, DC, pp. 927–932.
- Joukhader, A., Deguet, A., and Laugie, C. 1998. A collision model for rigid and deformable bodies. In *Proceedings of the IEEE International Conference on Robotics and Automation*, Leuven, Belgium, pp. 982–988.
- Kühnapfel, U., Çakmak, H. K., and Maass, H. 2000. Endoscopic surgery training using virtual reality and deformable tissue simulation. *Computers and Graphics* 24(5):671–682.
- Leaf, B. G. A. V. 1960. Models of the plain-knitted loop. *Journal of the Textile Institute Transactions*, pp. 49–58.
- Mason, M. T. 2001. *Mechanics of Robotic Manipulation*, MIT Press, Cambridge, MA.
- Nakagaki, H., Kitagaki, K., Ogasawara, T., and Tsukune, H. 1997. Study of Deformation and Insertion Tasks of a Flexible Wire. In *Proceedings of the IEEE International Conference on Robotics and Automation*, Albuquerque, NM, pp. 2397–2402.
- Pai, D. K. 2002. STRANDS: Interactive Simulation of Thin Solids using Cosserat Models. *Computer Graphics Forum* 21(3):347–352.
- Phillips, J., Ladd, A., and Kavraki, L. E. 2002. Simulated

- knot tying. In *Proceedings of the IEEE International Conference on Robotics and Automation*, Washington, DC, pp. 841–846.
- Picinbono, G., Delingette, H., and Ayache, N. 2001. Non-linear and anisotropic elastic soft tissue models for medical simulation. In *Proceedings of the IEEE International Conference on Robotics and Automation*, Seoul, Korea, pp. 1371–1376.
- Remde, A. and Henrich, D. 2000. Direct and inverse simulation of deformable linear objects. In *Robot Manipulation of Deformable Objects*, D. Henrich and H. Wörn, editors, Advanced Manufacturing Series, Springer-Verlag, Berlin, pp. 43–70.
- Rosenblum, R. E., Carlson, W. E., and Tripp, E. 1991. Simulating the structure and dynamics of human hair: modelling, rendering and animation. *Journal of Visualization and Computer Animation* 2(4):141–148.
- Taylor, P. M. 1990. *Sensory Robotics for the Handling of Limp Materials*, Springer-Verlag, Berlin.
- Terzopoulos, D. and Witkin, A. 1988. Deformable models—physically based models with rigid and deformable components. *IEEE Computer Graphics and Applications* 41–51.
- Terzopoulos, D., Platt, J., Barr, A., and Fleischer, K. 1987. Elastically deformable models. *Computer Graphics* 21(4):205–214.
- Timoshenko, S. 1955. *Strength of Materials, Part I: Elementary Theory and Problems*, D. Van Nostrand, Princeton, NJ.
- Villarreal, A. and Asada, H. 1991. A geometric representation of distributed compliance for the assembly of flexible parts. In *Proceedings of the IEEE International Conference on Robotics and Automation*, Sacramento, CA, pp. 2708–2715.
- Wakamatsu, H., Hirai, S., and Iwata, K. 1995. Modeling of linear objects considering bend, twist, and extensional deformations. In *Proceedings of the IEEE International Conference on Robotics and Automation*, Nagoya, Japan, pp. 433–438.
- Weil, J. 1986. The synthesis of cloth objects. *Computer Graphics* 20(4):49–54.
- Witkin, A. and Welch, W. 1990. Fast animation and control of non-rigid structures. *Computer Graphics Proceedings (SIGGRAPH 1990)*, Dallas, TX, pp.243–252.
- Yue, S. and Henrich, D. 2002. Manipulating deformable linear objects: sensor-based fast manipulation during vibration. In *Proceedings of the IEEE International Conference on Robotics and Automation*, Washington, DC, pp. 2467–2472.
- Zheng, Y. F., Pei, R., and Chen, C. 1991. Strategies for automatic assembly of deformable objects. In *Proceedings of the IEEE International Conference on Robotics and Automation*, Sacramento, CA, pp. 2598–2603.
- Zhuang, Y. and Canny, J. 2000. Haptic interaction of global deformations. In *Proceedings of the IEEE International Conference on Robotics and Automation*, San Francisco, CA, pp. 2428–2433.